

## U-Pb dating of pedogenic calcite near the Permian— Triassic boundary, Karoo Basin, South Africa

# Heriberto Rochín-Bañaga<sup>1,†</sup>, Robert A. Gastaldo<sup>2</sup>, Donald W. Davis<sup>1</sup>, Johann Neveling<sup>3</sup>, Sandra L. Kamo<sup>1</sup>, Cindy V. Looy<sup>4</sup>, and John W. Geissman<sup>5,6</sup>

<sup>1</sup>Jack Satterly Geochronology Laboratory, Department of Earth Sciences, University of Toronto, Toronto, Ontario M5S 3B1, Canada <sup>2</sup>Department of Geology, Colby College, Waterville, Maine 04901, USA

## **ABSTRACT**

We report U-Pb age determinations of carbonate nodules from an in situ paleosol horizon in the Upper Permian Balfour Formation and from several horizons of pedogenic nodule conglomerate (PNC) in the Triassic Katberg Formation, Karoo Basin, South Africa, using laser ablation-inductively coupled plasma-mass spectrometry (LA-ICP-MS). The paleosol sample yields an age of  $252 \pm 3$  Ma, which overlaps with a previous high-precision U-Pb zircon date from a volcanic ash deposit 2 m above the paleosol. This relationship demonstrates the reliability of using LA-ICP-MS dating techniques on terrestrial pedogenic calcite. Two PNC samples collected at the base of the Katberg Formation within the same sandstone unit vield ages of 255  $\pm$  3 Ma and 251  $\pm$  3 Ma. The age of  $251 \pm 3$  Ma overlaps with the high-precision U-Pb zircon date below the PNC and is a maximum age estimate of deposition for the base of the Katberg Formation. Our results show that reworked nodules in the same concentrated conglomerate lag can be of different ages, but that similarly aged nodules are spatially associated. In addition, two PNC samples collected higher in the section yield ages of 249  $\pm$  3 Ma and 241  $\pm$  3 Ma, providing maximum depositional ages for the lower to middle Katberg Formation for the first time. We demonstrate that pedogenic carbonate nodules can be dated with meaning-

Heriberto Rochín-Bañaga https://orcid.org/0000-0001-9253-7929

†heriberto.rochinbanaga@mail.utoronto.ca

ful precision, providing another mechanism for constraining the age of sedimentary sequences and studying events associated with the Permian-Triassic transition in the central Karoo Basin, even though the extinction boundary may not be preserved in this area.

#### INTRODUCTION

The end-Permian crisis represents the largest known mass extinction in Earth's history. It is reported to have affected ~90% of marine invertebrate species and is marked by the demise of conodonts, micro-gastropods, fusulinids, various brachiopods, echinoderms, molluscan clades, and other taxa (Erwin, 1994; Ogg, 2012; Shen et al., 2019; Dal Corso et al., 2022). The marine extinction event is recorded by high-resolution conodont zonation in the Permian-Triassic Global Boundary Stratotype Section and Point (GSSP) at Meishan, China, which is mainly defined by the first appearance datum of the conodont Hindeodus parvus (Chen et al., 2015). Here, high-precision U-Pb geochronology on zircons from several ash deposits indicates that the end-Permian extinction event occurred between  $251.941 \pm 0.037$  Ma and  $251.880 \pm 0.031$  Ma, which represents an interval of  $60 \pm 48$  ka (Burgess et al., 2014). A similar age for the marine event of  $251.939 \pm 0.031 \, \text{Ma}$  was found at Penglaitan, South China (Shen et al., 2019).

Several hypotheses propose that climate change due to increased atmospheric  $pCO_2$  from intense volcanism associated with the emplacement of the Siberian Traps was the main cause of biodiversity loss (Knoll et al., 1996; Brand et al., 2012; Burgess and Bowring, 2015; Burgess et al., 2017; Wu et al., 2021b). Other

proposed volcanism-related proximal causes include metal poisoning (Chu et al., 2021) and ozone depletion (Visscher et al., 2004; Black et al., 2014; Benca et al., 2018). The Siberian Traps, a large igneous province (LIP), is derived from one of the most voluminous and explosive volcanic series of events known in the Phanerozoic. It comprises a composite  $\sim$ 6500-m-thick sequence that was deposited over a period of less than 1 Ma (Kamo et al., 2003). U-Pb chemical abrasion-isotope dilution-thermal ionization mass spectrometric (CA-ID-TIMS) zircon ages indicate that magmatic activity at the Siberian Traps began between 252.47  $\pm$  0.14 Ma (Davydov et al., 2021) and 252.24  $\pm$  0.12 Ma (Burgess and Bowring, 2015), while the end of magmatic activity is estimated at  $250.2 \pm 0.3$  Ma (Kamo et al., 2003). The timing and duration of Siberian magmatism are consistent with events of the marine record.

Several authors have proposed that terrestrial ecosystems were affected at the same time as the marine crisis and experienced a similar degree of biodiversity loss (Twitchett et al., 2001; Ward et al., 2005; Viglietti et al., 2021; Wu et al., 2021a). The response of terrestrial ecosystems, the extent to which continental floras and faunas were affected, and the timing of that response continue to be debated (Davydov et al., 2021; Nowak et al., 2019; Vajda et al., 2020; Aftabuzzaman et al., 2021; Gastaldo et al., 2021; Lucas, 2021; Yang et al., 2021; Tabor et al., 2022). Although the marine Permian-Triassic boundary is well established, numerical age data that would help constrain the effects in and around the terrestrial Permian-Triassic boundary are limited and localized in just a few basins. The relative dearth of datable minerals in continental

GSA Bulletin; https://doi.published online 23 August 2023

https://doi.org/10.1130/B36968.1; 7 figures; 1 table; 1 supplemental file.

<sup>&</sup>lt;sup>3</sup>Council for Geosciences, Private Bag X112, Silverton, Pretoria 0001, South Africa

<sup>&</sup>lt;sup>4</sup>Department of Integrative Biology, Museum of Paleontology, University and Jepson Herbaria, University of California, Berkeley, 3060 Valley Life Sciences Building #3140, Berkeley, California 94720-3140, USA

<sup>&</sup>lt;sup>5</sup>Department of Geosciences, The University of Texas at Dallas, Richardson, Texas 75080-3021, USA

<sup>&</sup>lt;sup>6</sup>Department of Earth and Planetary Sciences, University of New Mexico, Albuquerque, New Mexico 87131-0001, USA

sedimentary rocks, especially zircon from airfall ash deposits, as well as the fact that continental successions are notoriously incomplete and difficult to correlate, hamper these attempts.

There are several continental basins across the planet for which geochronometric ages constrain the latest Permian and earliest Triassic successions that surround the end-Permian crisis. The Karoo Basin, South Africa, is considered to contain one of the most important continental sequences spanning the Permian-Triassic boundary and served as an early model for the terrestrial extinction event. This is due to its extensive and well-preserved paleontologic record of vertebrates (Ward et al., 2005; Viglietti et al., 2016, 2021; Gastaldo et al., 2019) and, to a much lesser extent, fossil plants (Prevec et al., 2010; Gastaldo et al., 2019) and pollen-andspore records (Barbolini et al., 2018; Gastaldo et al., 2020a). Here, geochronometric age constraints have demonstrated that diagnostic taxa previously used to define the post-extinction vertebrate fauna (Viglietti et al., 2021), and considered to be Early Triassic (Botha et al., 2020; Smith et al., 2022), are preserved in latest Changhsingian strata at  $252.24 \pm 0.11$  Ma (Gastaldo et al., 2020a). More recently, these same taxa were demonstrated to have coexisted across the same late Changhsingian landscapes as taxa diagnostic of the pre-extinction fauna, all of which thrived in vegetation dominated by the gymnosperm Glossopteris (Gastaldo et al., 2021). In recent years, the response of terrestrial ecosystems in Sydney Basin, Australia, has superseded the Karoo Basin as a model for this extinction event in Gondwana. The collapse of the Glossopteris-dominated plant communities in eastern Australia appears to have started earlier than any perturbation in the marine realm (Fielding et al., 2019; Mays et al., 2021), beginning at ca.  $252.31 \pm 0.07$  Ma (latest Changhsingian; Mays et al., 2020), with ecosystem disturbance in this part of the southern hemisphere extending into the Olenekian (Fielding et al., 2021; Mays et al., 2021).

The pattern of vegetational change occurring hundreds of thousands of years before the marine extinction event is not repeated at other paleolatitudinal positions, but there is ample evidence of several perturbations in the floral realms starting in the Late Permian up to the Middle Triassic (Hermann et al., 2011). For example, collapse of terrestrial and marine ecosystems in Greenland occurred synchronously, but the extinction of characteristic Permian plant taxa is phased (Looy et al., 2001; Twitchett et al., 2001). In the fully continental record outcropping in the North China Block, Bogda Mountains, China (Yang et al., 2021), vegetational turnover occurred during the early Induan (ear-

liest Triassic, 251.9–251.2 Ma), which postdates the marine event. Evidence for a continuous record of riparian vegetation and upland forests occurs in this rift-basin setting into the early Olenekian (251.2–247.2 Ma). Similarly, the fully continental succession in the Kuznetsk Basin, Russia, shows no evidence of an end-Permian vegetational extinction. Rather, this basin documents the extirpation of a humid-dominated cordaitean flora at ca. 820 ka prior to the marine event, with subsequent floristic diversification across the Permian–Triassic transition (Davydov et al., 2021).

Only precise geochronology makes it possible to understand the patterns preserved in the stratigraphic record, and high-precision numerical age data, thus far, have depended on the presence of zircon in ash-fall deposits. Deposition of such material requires nearby volcanism and, once deposited, the probability for preservation of these mostly fine-grained fall deposits is low due to continual reworking (e.g., phyto- and bioturbation in soils and ongoing fluvial and erosional processes), which is common in terrestrial systems (Rasmussen et al., 2021). Unlike ash-fall deposits, carbonate material is abundant in both marine and continental depositional environments, precipitating either as primary and/ or secondary mineral phases, and is preserved throughout an extensive geologic record. On land, pedogenic (soil-precipitated) carbonate minerals form mostly in regions of seasonally dry climate (Railsback, 2021), but they are also reported from humid environments (Sheldon and Tabor, 2009) and, since the early Cenozoic, from grasslands (Retallack et al., 2002). Pedogenic carbonates have been used to reconstruct deeptime paleoclimate. Using geochemical properties, including stable carbon and oxygen isotopes (Leone et al., 2000; Retallack, 2005), it is possible to determine whether a paleosol developed under seasonally wet-and-cool or warm-anddry conditions (Tabor et al., 2022; Sheldon and Tabor, 2009; Gastaldo et al., 2020b). In addition, it is possible to derive estimates of atmospheric pCO<sub>2</sub> at the time of calcite precipitation from calcite-cemented soil nodules (Gastaldo et al., 2014; Joachimski et al., 2022).

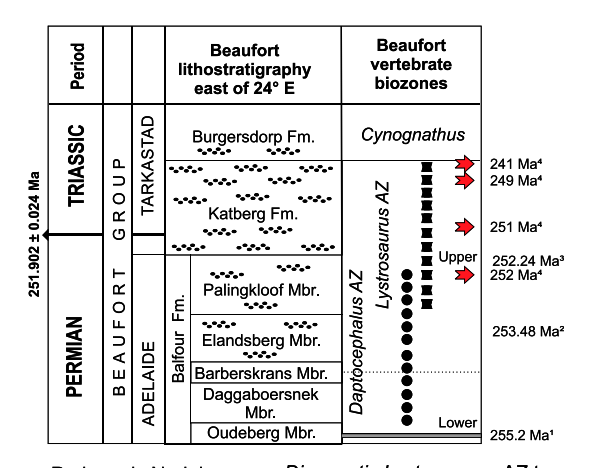
Calcite-bearing paleosols incorporate uranium at the time of mineral precipitation (Jahn and Cuvellier, 1994; Rasbury and Cole, 2009). Therefore, a U-Pb age can be calculated for the time of soil formation provided that the ratios of U to initial common Pb concentrations are high enough and the carbonate was not affected by late diagenetic alteration. Secondary calcite normally precipitates with a low-U content and a significant common Pb component, making it a challenge to obtain accurate and precise U-Pb ages. However, recent advances in laser abla-

tion-inductively coupled plasma-mass spectrometry (LA-ICP-MS) and Bayesian statistical analysis extend the range of samples that can be usefully dated (Roberts et al., 2020; Davis and Rochín-Bañaga, 2021). We present results of the application of these techniques to pedogenic calcite nodules obtained from one paleosol and several pedogenic nodule conglomerates (PNC) from the Balfour and Katberg formations. The paleosol interval has been inferred to straddle the Permian-Triassic extinction boundary in the Karoo Basin, South Africa. Currently, our understanding of the timing and duration of this critical interval in this basin has been limited by the dearth of volcanic deposits. However, U-Pb LA-ICP-MS dating of pedogenic calcite has the potential to provide direct timing of the events surrounding the Permian-Triassic extinction, even when this boundary may not be preserved in the central part of the Karoo Basin.

## GEOLOGIC BACKGROUND

The Karoo Basin is considered to represent a large subsiding retroarc foreland basin (Catuneanu et al., 2005; Smith et al., 2020) that contains a succession of upper Paleozoic deglacial sedimentary rocks overlain mainly by fully continental deposits known as the Karoo Supergroup. Sedimentary rocks resulting from deglaciation are found in the basal Dwyka (upper Carboniferous) and Ecca (Lower-middle Permian) groups, with a transition to fully continental deposits in the Beaufort (Permian-Triassic) and Stormberg groups (Triassic-Jurassic). The Beaufort Group is subdivided into two subgroups: the lower Adelaide and upper Tarkastad. The depositional setting of the Balfour Formation (Fig. 1), the uppermost unit of the Adelaide subgroup that is postulated to span the Permian-Triassic transition, is interpreted as fluvial-lacustrine with intervening paleosols having various weathering characteristics (Gastaldo et al., 2014, 2020b). Paleosols from the uppermost exposures of this unit formed under conditions that fluctuated from relatively humid (Ward et al., 2000) and cool to seasonally dry and warm (Gastaldo et al., 2020c).

The overlying Tarkastad subgroup is subdivided into the arenaceous Katberg and argillaceous Burgersdorp formations. The Katberg Formation is traditionally interpreted to represent fluvial systems deposited under more seasonally dry to semiarid conditions (e.g., Ward et al., 2000; Pace et al., 2009). It consists of a monotonous succession of fine- to very finegrained feldspathic wacke fining upward into mottled mudrock, and has been the focus of different paleontologic studies because of its extensive fossil record. Therapsid fossils, including *Lystrosaurus murrayi* and *L. declivis*, are abun-



- Pedogenic Nodule Conglomerate (PNC)
- Diagnostic Lystrosaurus AZ taxaDiagnostic Daptocephalus AZ taxa
- to Middle Triassic succession. Geochronometric age constraints for stage boundaries follow the International Chronostratigraphic Chart v2022/10 (www.stratigraphy.org) with (1) the base of the *Daptocephalus* Assemblage Zone (AZ) after Rubidge et al. (2013); (2) the age constraint on the Elandsberg Member (Mbr.) after Gastaldo et al. (2015, 2018); (3) the age on the upper Palingkloof Member after Gastaldo

et al. (2020a); the placement of

Figure 1. Generalized stratig-

raphy of the Karoo Basin with

a focus on the Upper Permian

the Permian-Triassic Boundary in the Katberg Formation after Gastaldo et al. (2020a, 2015, 2017); and (4) age constraints for the Katberg Formation as exposed on Farm Nooitgedacht presented herein. The uncertainty surrounding whether a boundary exists between the traditional lower and upper *Daptocephalus* AZ (Viglietti et al., 2016) and an overlying *Lystrosaurus declivis* AZ (Botha and Smith, 2020) follows Gastaldo et al. (2021).

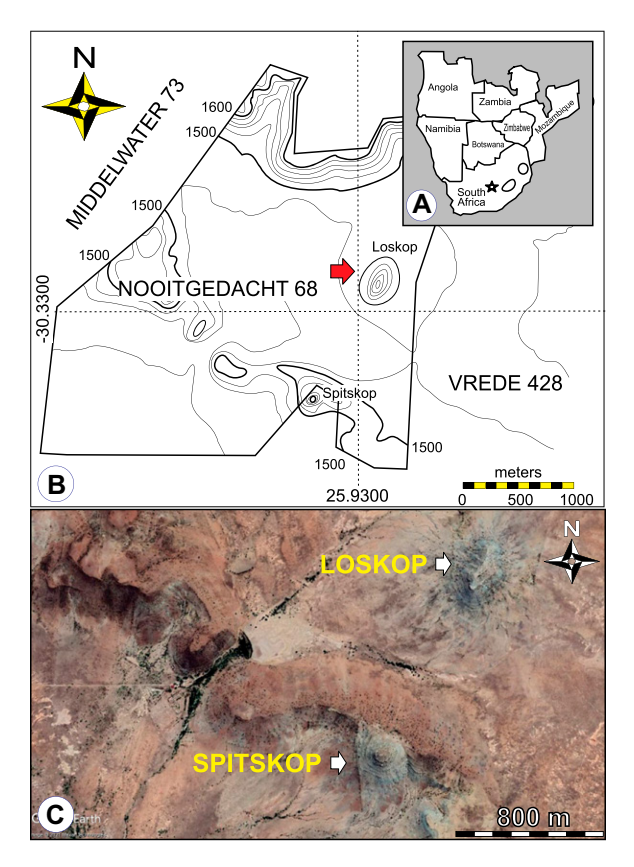
dant and well preserved throughout the formation (Smith and Botha-Brink, 2014; Smith et al., 2022). These fossils were previously used as diagnostic taxa to delimit the L. declivis Assemblage Zone (AZ; Botha and Smith, 2020) and, in part, the Katberg Formation itself. Recently, it was demonstrated empirically that diagnostic taxa reported to have their first appearance datum in the Triassic coexisted with the diagnostic taxa of the underlying Daptocephalus AZ in glossopterid-dominated latest Permian landscapes (Gastaldo et al., 2021). Based on a combination of geochronologic, magnetic polarity stratigraphic, and palynological evidence, the Permian-Triassic transition has been placed in the Katberg Formation (Gastaldo et al., 2020a, 2021).

### MATERIALS AND METHODS

## **Locality and Samples**

The sampling locality is located ~20 km north–northwest of the town of Bethulie in the southern Free State Province (S 30.32530°, E 025.93132°), South Africa, on Farm Nooitgedacht 68 (Fig. 2). Fieldwork focused on the koppie (butte) Loskop (Fig. 3A), which rises ~100 m above a plain with its talus-covered flanks consisting of horizontal beds of blocky fine–very fine feldspathic wacke, weathered and friable mudrock varying in color from greenishgray (5GY 6/1) to grayish-brown (5 YR 4/2), along with scattered colluvium, including pedogenic nodules and vertebrate bone fragments. Measured sections are facilitated by a series of

erosional scars (dongas) with typically excellent exposure (Gastaldo et al., 2020a), and resistant sandstone bodies that traverse the koppie and are used to constrain depositional units (Fig. 3B). Lenses of PNC lag deposits appear sporadically



at the bases of channel sandstone bodies exposed in the upper part of the koppie (Fig. 3B). These lag deposits mark erosional basal unconformities in the succession, with the calcite-cemented pedogenic nodules representing residuum from landscape degradational processes (Gastaldo and Demko, 2011). Lags, which also contain abundant bone fragments, have concentrated these recalcitrant soil nodules from eroded paleosols, including vertisols (Gastaldo et al., 2020b, 2020c). All PNC-bearing sandstones exposed across the Loskop and Spitskop koppies (Fig. 2B) are assigned to the Katberg Formation (Botha-Brink et al., 2014, 2020; Gastaldo et al., 2020a).

Five PNC samples and one paleosol were collected and analyzed in this study (Fig. 4). The paleosol sample (NGT9-6) was collected in situ from a red siltstone unit  $\sim$ 2–3 m below the stratigraphic position from which the 252.24  $\pm$  0.11 Ma zircon age is reported (Fig. 3C; Gastaldo et al., 2020a; their fig. 2).

Two samples, NGT9-7 and NGT9-8, originate from the lowest PNC-bearing sandstone bed in the section, which is  $\sim$ 7 m above the thin ash-fall deposit yielding the 252.24  $\pm$  0.11 Ma zircon age (Gastaldo et al., 2020a). NGT9-7 and NGT9-8 were collected in situ, and each sample comes from a different part of the same lag

Figure 2. Location of Farm Nooitgedacht, Free State Province, South Africa, where pedogenic nodules were sampled from intraformational conglomerate deposits occurring as fluvial lags in the Katberg Formation. (A) Map of southern Africa; a star indicates the location of the farm. (B) Contour map of Farm Nooitgedacht (S 30.32530°, E 025.93132°; after Gastaldo et al., 2020a) showing exposed uppermost Permian and Lower Triassic intraformational conglomerate, sandstone, mudstone on two small buttes (koppie). Devitrified claystone (ash-fall deposit) from which a concordant U-Pb chemical abrasion-isotope dilution-thermal ionization mass spectrometric (CA-ID-TIMS) single crystal zircon age of  $252.24 \pm 0.11$  Ma was obtained crops out on Loskop. Pedogenic nodule conglomerate was collected from Loskop (red arrow). (C) Google Earth image of Farm Nooitgedacht. Scales are in meters.

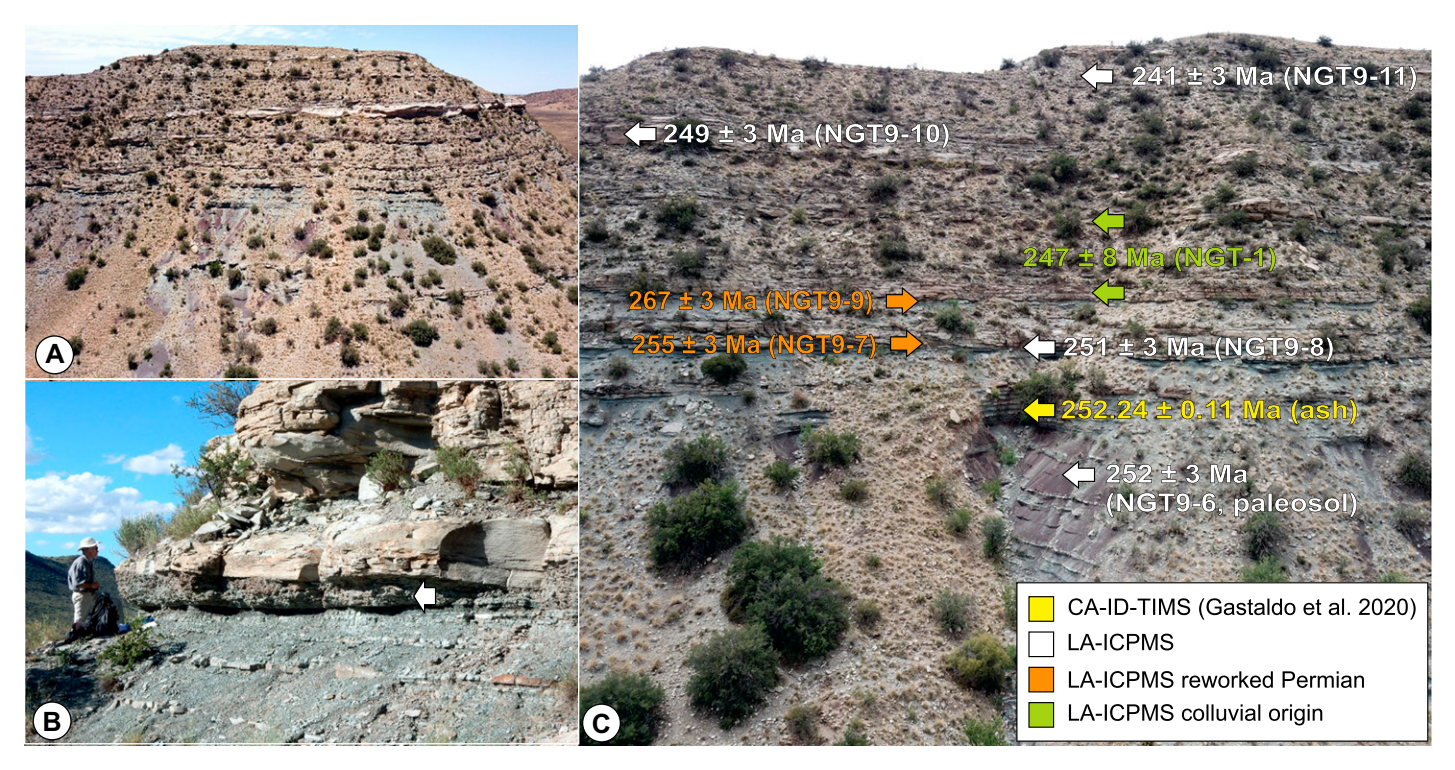


Figure 3. Loskop koppie on Farm Nooitgedacht. (A) Drone image of western exposure where intraformational pedogenic nodule conglomerate (PNC) occurs as intermittent lag deposits at the base of sandstone bodies. Here, the Katberg Formation is composed of thin sheet sandstones with one thick channel-form body attaining a thickness of <8 m. (B) Image of lowest exposed PNC lag deposit (samples NGT9-7 and NGT9-8) positioned  $\sim$ 1 m stratigraphically above the devitrified volcanogenic ash-fall deposit from which a concordant U-Pb chemical abrasion—isotope dilution—thermal ionization mass spectrometric (CA-ID-TIMS) age of 252.24  $\pm$  0.11 Ma has been reported (Gastaldo et al., 2020a). (C) Stratigraphic positions and laser ablation—inductively coupled plasma—mass spectrometric (LA-ICP-MS) age estimates of calcite nodules from a paleosol and PNC lag deposits.

accumulation at the base of this channel body; hence, these are lateral equivalents (Fig. 3C). In contrast, NGT-1 was collected from colluvium at the base of the Loskop cliff face below where the thickest sandstone body is exposed (Fig. 3C). Calcitic nodules in these samples range from  $\sim$ 2 mm to 6 mm in diameter, vary in shape from rounded to subrounded, and are enclosed in a fine-grained sand matrix in which fragmented bone, rip-up mudclasts, and mud aggregates also occur (Pace et al., 2009; Gastaldo et al., 2013). The PNC sample NGT9-9 was collected from a 1.5-m-thick greenish-gray siltstone, whereas samples NGT9-10 and NGT9-11 were collected higher, from PNC lenses bounding fine-grained sandstone benches (Fig. 3C; Table 1).

## **Analytical Methods**

U-Pb isotopic analyses were conducted at the University of Toronto using an Agilent 7900 ICPMS and an NWR193 excimer laser system. U-Pb data (<sup>238</sup>U, <sup>206</sup>Pb, and <sup>207</sup>Pb) were collected using scan-lines over individual nodules resulting in hundreds of cycle data per line (Drost et al., 2018; Hoareau et al., 2021; Davis and

Rochín-Bañaga, 2021). <sup>230</sup>Th was also monitored to check for detrital contamination but was found to be uniformly low.

Targeted nodules show massive matrices and were selected randomly. Each scan-line analysis, 4–5 mm long, was pre-ablated at a fast scan rate, 200  $\mu m/s$ , and high frequency, 20 Hz, using a larger diameter beam (150  $\mu m$ ) to remove surface contamination. U-Pb line analyses were conducted with a fluence of  $\sim\!4.5$  J/cm², beam diameter of 120  $\mu m$ , and frequency of 10 Hz at a rate of 15  $\mu m/s$ . Baselines were accumulated on each scan-line for 20 s prior to opening the laser. The depth of the scan-line is  $\sim\!10$ –20  $\mu m$ . LA-ICP-MS parameters for U-Pb analyses are provided in Table S1 in the Supplemental Material¹. U decay constants are from Jaffey et al.

(1971), and the  $^{238}$ U/ $^{235}$ U ratio is taken as 137.88 (Steiger and Jäger, 1977).

Both the glass standard NIST612 and Duff Brown Tank were used to correct for mass and oxide elemental fractionation bias. The uncertainty of our U-Pb ages includes measurement errors in mass signals from the sample NIST612, and Duff Brown Tank calcite-standard measurements. The Duff Brown Tank standard was used as a matrix-matched reference. Ages have been corrected by an ablation bias factor of 1.03 based on comparison of the measured age of Duff Brown Tank of  $62 \pm 1$  Ma (mean square of weighted deviates [MSWD] = 0.68; Y intercept fixed at 0.738) with its ID-TIMS age of  $64.04 \pm 0.67$  Ma (Hill et al., 2016). An additional calcite standard (Walnut Canyon standard, WC-1) with an ID-TIMS age of 254.4  $\pm$  6.4 Ma (Roberts et al., 2017) was measured to provide control on accuracy and precision. The age of WC-1 was measured at 254  $\pm$  3 Ma (2 $\sigma$ , MSWD = 0.68) with a fixed  $^{207}$ Pb/ $^{206}$ Pb ratio of 0.85, after correction using the factor of 1.03. Tera-Wasserburg concordia diagrams from the Duff Brown Tank and WC-1 standards can be found in the Supplemental Material.

<sup>&</sup>quot;Supplemental Material. The supplemental material contains the LA-ICP-MS parameters for U-Pb analyses, the Tera-Wasserburg concordia diagrams for the calcite standards, and the Utilchron Excel files used for data processing and age regressions from individual samples. Please visit https://doi.org/10.1130/GSAB.S.23638722 to access the supplemental material, and contact editing@geosociety.org with any questions.

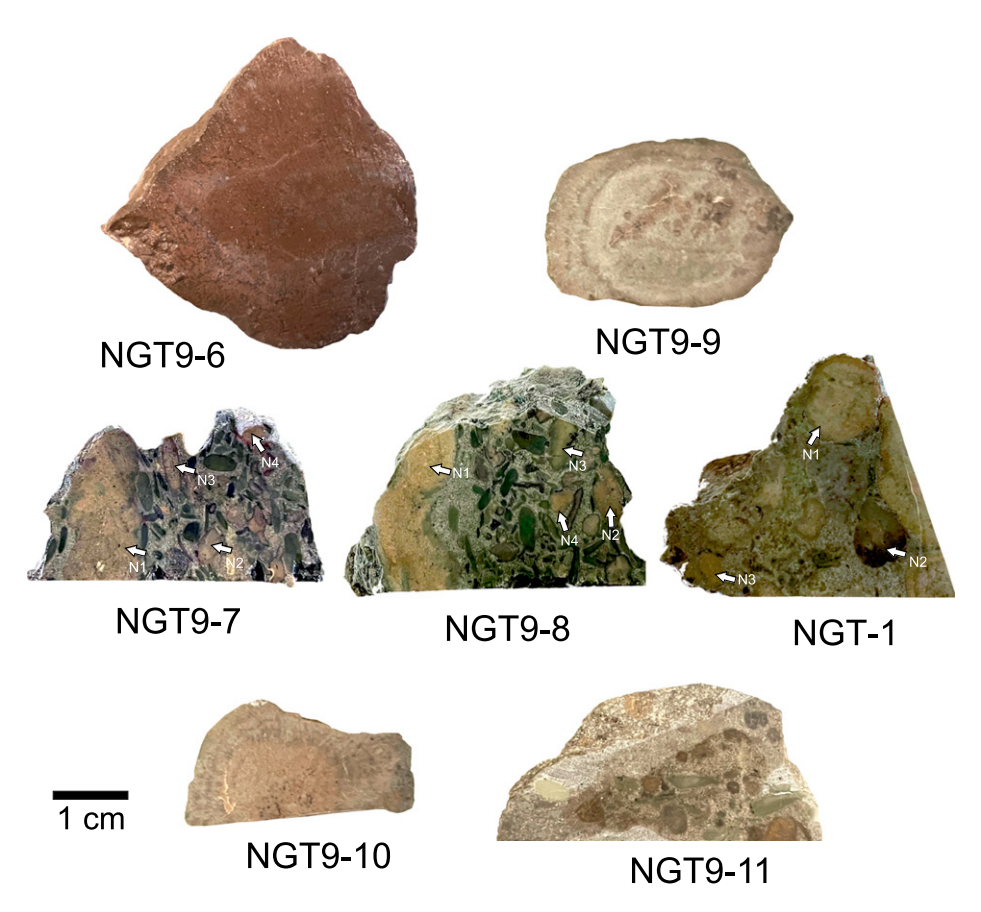


Figure 4. Calcite nodule samples from the pedogenic nodule conglomerate at Farm Nooitgedacht, Karoo Basin. Scale bar is 1 cm. White arrows indicate the nodules selected for U-Pb laser ablation-inductively coupled plasma-mass spectrometric (LA-ICP-MS) dating.

TABLE 1. LASER ABLATION-INDUCTIVELY COUPLED PLASMA-MASS SPECTROMETRIC U-Pb AGE RESULTS FROM PEDOGENIC NODULE SAMPLES FROM THE KATBERG FORMATION, FARM NOOITGEDACHT, FREE STATE PROVINCE, SOUTH AFRICA

Sample	Samples coordinates	<sup>238</sup> U (ppm)	<sup>206</sup> Pb (ppm)	Th/U	Age (Ma)	MSWD	<sup>207</sup> Pb/ <sup>206</sup> Pb (PbC)
NGT9-6	S 30.32603°, E 26.93248°	22.0	13.0	0.2	$252 \pm 2.8$	2.4	$0.832 \pm 0.007$
NGT9-7	S 30.32530°, E 25.93132°	Weighted mean age =			$254 \pm 2.9$	0.6	
Nodule 1		30.2	5.5	0.1	$253\pm7$	1.7	$0.833 \pm 0.013$
Nodule 2		20.4	10.7	0.2	$258 \pm 6$	1.2	$0.844 \pm 0.008$
Nodule 3		43.6	8.0	0.1	$253\pm7$	1.2	$0.830 \pm 0.012$
Nodule 4		43.1	6.2	0.1	$254\pm 5$	2.4	$\textbf{0.838} \pm \textbf{0.004}$
NGT9-8	S 30.32530°, E 25.93132°	Weighted mean age =			$251 \pm 2.6$	0.5	
Nodule 1		42.3	8.7	0.1	$250\pm7$	1.3	$0.839 \pm 0.012$
Nodule 2		33.4	6.9	0.1	$248\pm7$	1.3	$0.820 \pm 0.008$
Nodule 3		62.9	11.7	0.2	$252 \pm 5$	1.2	$0.833 \pm 0.013$
Nodule 4		20.8	5.7	0.1	$252\pm4$	1.3	$\textbf{0.840} \pm \textbf{0.009}$
NGT-1							
Nodule 1		19.0	4.7	0.1	$268 \pm 5$	2.0	$0.809 \pm 0.007$
Nodule 2		43.9	5.7	0.0	$247 \pm 8$	1.1	$\textbf{0.805} \pm \textbf{0.008}$
Nodule 3		23.0	5.9	0.2	$268\pm12$	1.3	$\textbf{0.849} \pm \textbf{0.009}$
NGT9-9	S 30.32569°, E 25.93307°	30.0	9.1	0.1	$267 \pm 2.6$	1.7	$\textbf{0.834} \pm \textbf{0.007}$
NGT9-10	S 30.32592°, E 25.93287°	29.0	4.3	0.1	$249 \pm 2.9$	1.0	$0.828 \pm 0.008$
NGT9-11	S 30.32611°, E 25.93314°	18.1	8.3	0.2	$241\pm3.3$	2.0	$\textbf{0.833} \pm \textbf{0.007}$

 $\it Note: MSWD-mean square of weighted deviates; PbC-^{207}Pb/^{206}Pb, isotopic composition of the initial common Pb component.$ 

### **Data Processing**

Excel data sheets with results, errors, and software for regressions, as well as instructions for repeating calculations, are given in the Supplemental Material. Calcite minerals usually contain significant common as well as radiogenic Pb. Hence, age determinations are based on defining a mixing line in isotope-ratio space whose intersection with the concordia (curve showing radioactive equilibrium at a given age) shows the age of the radiogenic component while its Y (207Pb/206Pb)-axis intercept on the Tera-Wasserburg plot gives the isotopic composition of the initial common Pb component (denoted PbC). Mixing lines are defined using a data set, or multiple data sets, from samples similar in age and PbC. Data were processed as single measurement cycles to exploit the maximum U/Pb spread along the mixing line.

U-Pb regression was carried out using a Bayesian statistical program (Utilchron) that regresses mass-count data with 1-sigma absolute errors  $(1/\sqrt{N})$ , where N is the total count number) in a 3-D signal space (Davis and Rochín-Bañaga, 2021). Details of data processing and regressions are given for individual samples in Utilchron Excel files in the Supplemental Material data. These files contain detailed instructions for use. U-Pb data are also regressed using conventional least-squares regression of ratios (Isoplot; Ludwig, 2012) for comparison purposes and to determine the MSWD. U-Pb data are plotted and regressed using Tera-Wasserburg (inverse) concordia diagrams, where (1) the age represents the intersection of the best-fit line with the concordia curve and (2) PbC is given by its Y-axis intercept. Data sets consist of hundreds of measurements; as such, error ellipses are not shown but are taken into account in the calculations. Errors on age and initial <sup>207</sup>Pb/<sup>206</sup>Pb are quoted at 95% confidence (2 sigma). Tera-Wasserburg (inverse) concordia diagrams from the pedogenic nodules are found in Figures 5 and 6.

## RESULTS AND DISCUSSION

U-Pb LA-ICP-MS data from the paleosol pedogenic nodules and pedogenic nodule conglomerate lags are presented in Table 1 and Figures 5 and 6. The paleosol sample shows U and Pb content of 22 ppm and 13 ppm, respectively. The U content in nodules collected in channel lag deposits varies from 19 ppm to 63 ppm, with <sup>206</sup>Pb/<sup>238</sup>U in the range of 0.13 and 0.52. The paleosol and PNC nodules have low-Th/U values due to the insolubility of Th in aqueous solutions, which should also be of low concentration in diagenetic fluids.

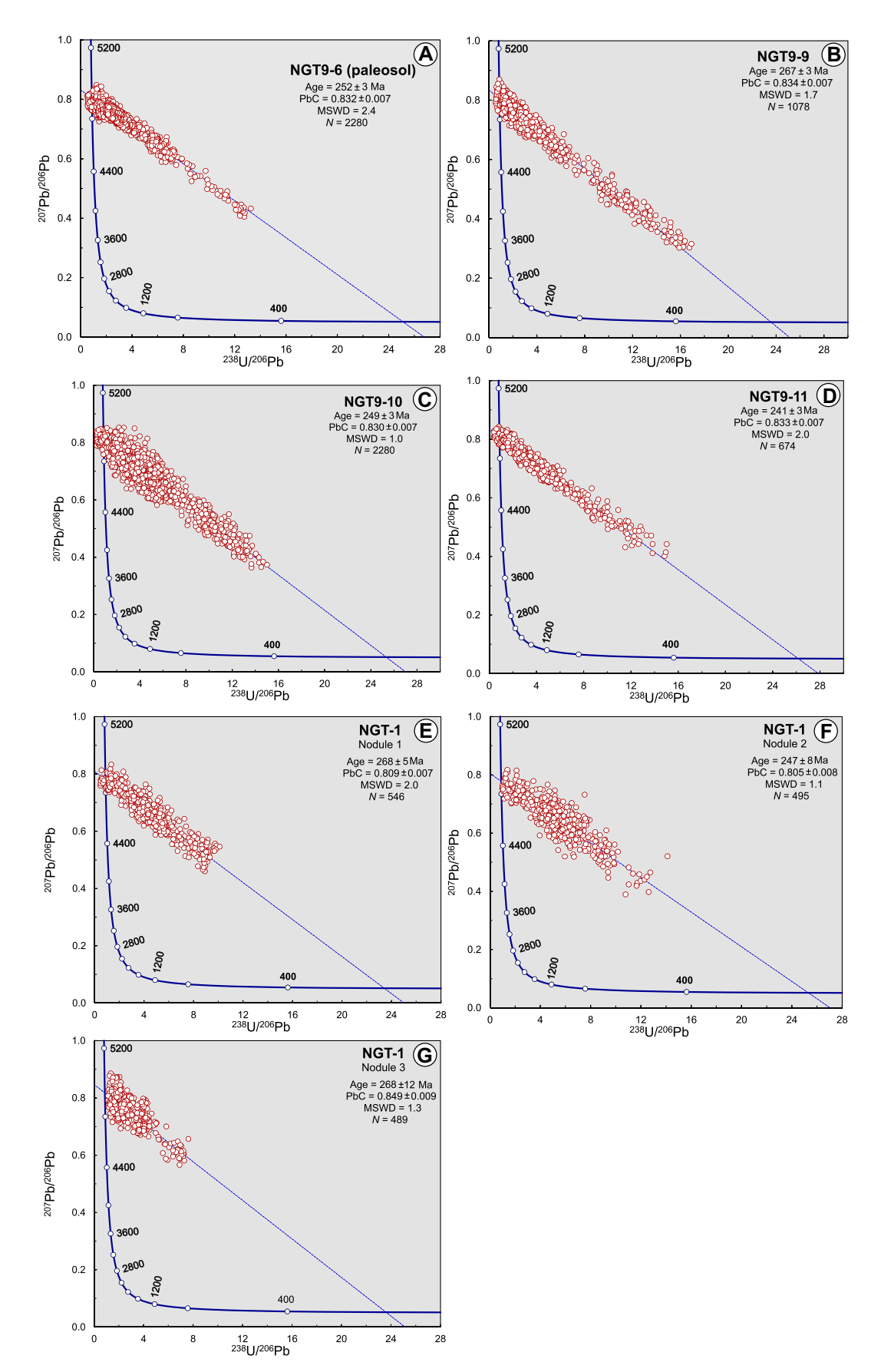
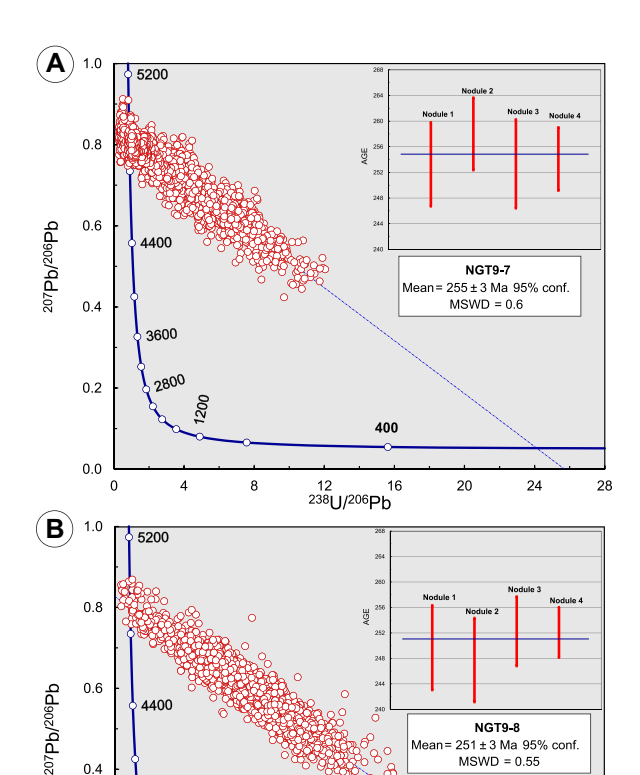


Figure 5. Tera-Wasserburg concordia diagrams from the paleosol (NGT9-6) and pedogenic nodule conglomerate (PNC) samples (NGT9-9, NGT9-10, NGT9-11, and NGT-1) as well as age results and mean age of nodules collected from two locations within the same PNC lag deposit (NGT9-7 and NGT9-8). MSWD—mean square of weighted deviates.



12 16 238[J/206Pb

MSWD = 0.55

Tera-Wasserburg 6. concordia diagrams and mean age of nodules collected from two locations within the same pedogenic nodule conglomerate (PNC) lag deposit (NGT9-7 and NGT9-8). MSWD-mean square of weighted deviates.

The NGT9-6 paleosol sample yields an age of  $252 \pm 3$  Ma with a PbC of 0.832 (Fig. 5A). Individual nodules from PNC sample NGT9-7 yield overlapping ages of  $253 \pm 7$  Ma,  $258 \pm 6$  Ma,  $253 \pm 7$  Ma, and  $254 \pm 5$  Ma (Fig. 6A). The nodules from NGT9-8 within the same lag also yield overlapping ages of  $250 \pm 7$  Ma,  $248 \pm 7 \text{ Ma}, 252 \pm 5 \text{ Ma}, \text{ and } 252 \pm 4 \text{ Ma}$ (Fig. 6B). All nodules show overlapping PbC values ranging from  $0.820 \pm 0.008$  to  $0.844 \pm 0.008$ . These values are approximately consistent with the average crustal model-based common Pb for this age (~0.85; Stacey and Kramers, 1975). The weighted mean <sup>238</sup>U/<sup>206</sup>Pb age and 95% confidence errors for NGT9-7 are  $255 \pm 3 \text{ Ma}$  (MSWD = 0.6), whereas those for NGT9-8 are  $251 \pm 3$  Ma (95% confidence, MSWD = 0.5). These two average ages do not agree within error (MSWD = -3.1). Although the eight individual measurements yield an average with a much lower MSWD of 0.9, ages from NGT9-7 are consistently older than those from NGT9-8, and data sets from NGT9-7 are also consistently less radiogenic (Fig. 6). This suggests that the nodules from each sample are from different sources with slightly different

0.2

ages. Since the nodules are all detrital, it is possible that even those from the same sample are different.

A suggestion that this may be so is that regressing all four data sets from NGT9-8 gives a best-fit age of  $246 \pm 3$  Ma, which is notably younger than the average of the four ages. The hypothesis used in regression is that all data scatter around a line defined by a single age and PbC value. Otherwise, results may be biased. For example, suppose that one were averaging two sets of data from samples having the same age but different PbC values. If one set is less radiogenic than the other and has a lower PbC value, then the average isochron through the more radiogenic data will be biased toward a lower Y intercept, which will cause the age to appear too young. Therefore, one should not combine data sets from different samples unless there is good evidence that they are uniform in age and PbC. It is better instead to average the ages from the separate regressions. The average ages from NGT9-7 and NGT9-8 within the same lag deposit, although not identical, are close and appear to be closer for the four nodules within each sample. This suggests a short transport distance with little opportunity for mixing between nodules from different horizons.

The detrital nodule from the higher level PNC sample NGT9-9 yields an age of 267  $\pm$  3 Ma with a PbC value of  $0.834 \pm 0.007$  (Fig. 5B). This age is older than the succession exposed at Nooitgedacht and likely represents the reworking of older sediment into the Katberg Formation. Samples NGT9-10 and NGT9-11 represent the highest samples from the section (Fig. 3C), and their nodules give the youngest ages of  $249 \pm 3$  Ma and  $241 \pm 3$  Ma, respectively, with PbC values of  $\sim$ 0.83 (Figs. 5C and 5D).

Three nodules from the colluvium sample NGT-1 yield ages of  $268 \pm 5$  Ma,  $247 \pm 8$  Ma, and  $268 \pm 12$  Ma with statistically distinct PbC values of  $0.809 \pm 0.007$ ,  $0.805 \pm 0.008$ , and  $0.849 \pm 0.009$ , respectively (Figs. 5E–5G). Since they were eroded from the thick sedimentary section exposed in the adjacent scarp, it is not surprising that they represent different generations with different ages and fluid sources.

PNC lags are common across the Balfour and Katberg formations (Pace et al., 2009; Viglietti et al., 2017; Gastaldo et al., 2018) and were once considered as a diagnostic criterion for identifying the latter in the Karoo Basin (e.g., Ward et al., 2000, 2005; Smith and Botha-Brink, 2014). The base of each intraformational nodule conglomerate represents an erosional contact of a newly established channel system associated with landscape degradation (Gastaldo and Demko, 2011). The establishment of new channel systems and associated interfluvial deposits throughout the Late Permian and Early Triassic was a consequence of changes in the fluvial gradient in the basin associated with climatic oscillations and tectonism. Each channel regime and the intervening paleosols that developed across the floodplain mark the initiation of an aggradational phase of deposition (Gastaldo et al., 2020a, 2020b) in which primarily entisols and vertisols formed. As aggradation slowed and landscapes reached stasis, vertisols developed in which calcite-cemented nodules could have precipitated. The stable carbon and oxygen isotopic composition of the calcite cement reflects whether mineralization occurred under closed-(Tabor et al., 2007) or open-system (Gastaldo et al., 2014) conditions. With the initiation of a subsequent degradational phase and erosion of the landscape, fine-grained detritus (sand and mud) was re-entrained in rivers and transported farther basinward to a different depocenter. In contrast, coarser detritus-granule, pebble, and cobble-sized pedogenic nodules-was retained as bedload lag deposits at the bases of channels and represents the incompetent sediment load associated with these river systems. Hence, calcite-cemented nodules recovered from chan-

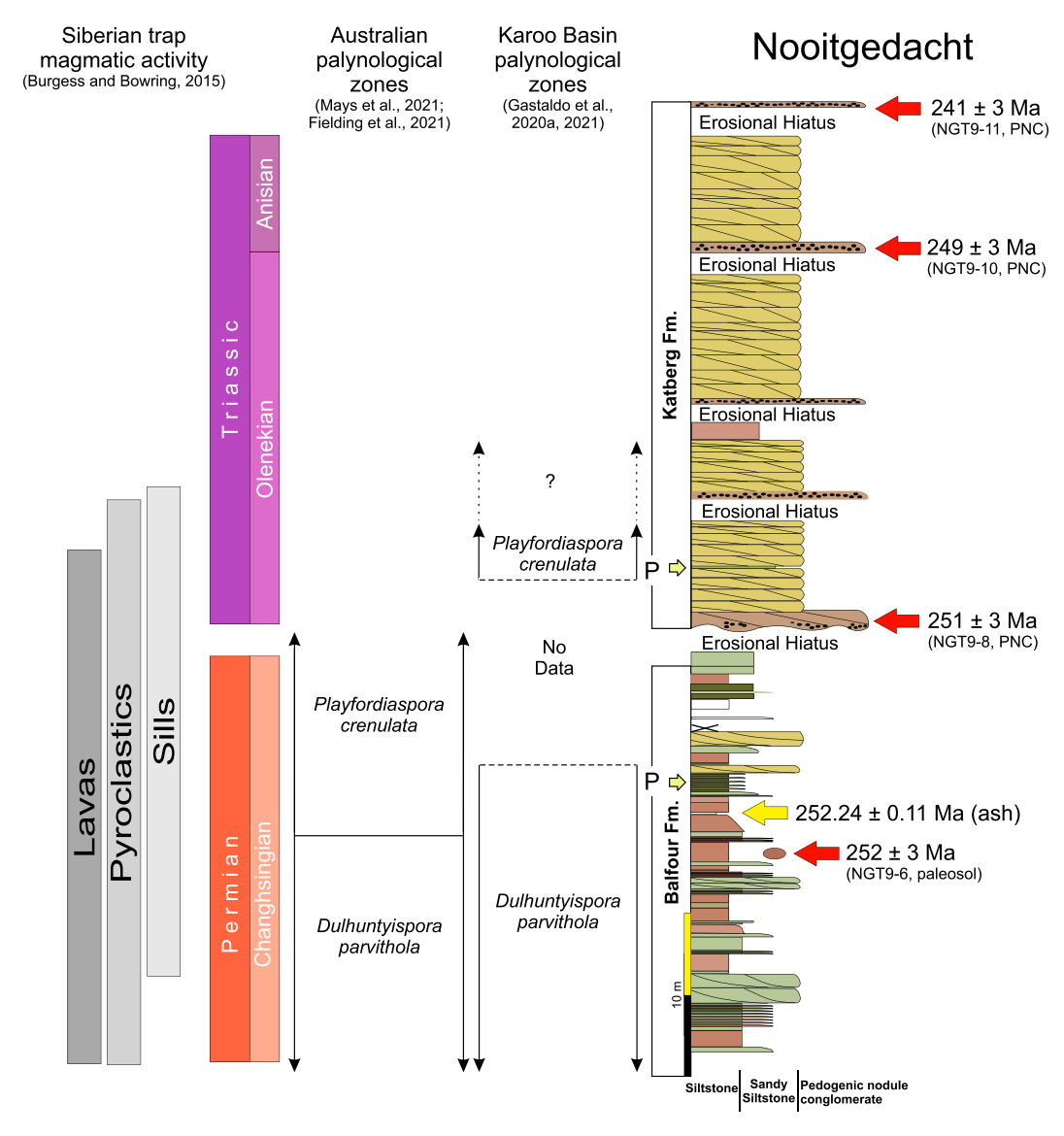


Figure 7. Geochronometric constraints of lithostratigraphic units on Farm Nooitgedacht. Geochronometric constraints are plotted against the palynological zones of the southern hemisphere in the Karoo Basin (Gastaldo et al., 2020a, 2021) and eastern Australia (Fielding et al., 2021; Mays et al., 2021). Correlation of the lithostratigraphy outcropping on Farm Nooitgedacht with the Geologic Time Scale (v2022/10). Permian-aged rocks are constrained by an age date of  $252.24 \pm 0.11$  Ma in the upper Balfour Formation, which is latest Changhsingian. The assigned age overlying Triassic (Induan; red arrow) rocks is constrained by our U-Pb laser ablation-inductively coupled spectrometric plasma-mass (LA-ICP-MS) maximum depositional age from calcitecemented pedogenic nodules overlying an erosional unconformity above the devitrified volcanogenic bed (yellow arrow). Due to the uncertainty of the original stratigraphic position of sample NGT-1, two possible positions of the maximum age assignment for Olenekian deposits are shown. See Figure 3 for horizons from which Olenekian and Ladinian age estimates were obtained. The age

ranges of Siberian Trap mafic lavas, pyroclastic deposits, and related mafic sills are based on Burgess and Bowring (2015). Fm.—formation; PNC—pedogenic nodule conglomerate. P. marks the palynological assemblages.

nel lag deposits represent, with a few exceptions, the only remnants of the "ghost" landscapes of the Karoo (Gastaldo et al., 2020c). These lag deposits provide the only insight into processes that operated across the landscape for which no stratigraphic record is preserved.

The age estimate of  $252 \pm 3$  Ma from the in situ paleosol nodule is in good agreement with the ash-fall deposit dated by Gastaldo et al. (2020a) at  $252.24 \pm 0.11$  Ma (Fig. 7). This suggests that the U-Pb system in the paleosol remained stable and unaffected by later depositional and diagenetic processes. The PNC lag at the base of the lowest channel sandstone body at Farm Nooitgedacht, assigned to the Katberg Formation, was sampled  $\sim 7$  m above the ashfall deposit (Fig. 7). The average age estimate of

 $251 \pm 3$  Ma for the group of four nodules from NGT9-8 represents a maximum age estimate for genesis of the nodules and their deposition in this PNC lag deposit. This Late Permian–Early Triassic age estimate agrees with that of the in situ paleosol as well as the inferred stratigraphic age assigned to the Katberg Formation based on the palynological record (Gastaldo et al., 2020a; Mays et al., 2021). Most importantly, it agrees with the high-precision U-Pb zircon date from the subjacent ash deposit, which demonstrates the integrity of the U-Pb dating technique (Fig. 7).

Although it lacks a well-constrained stratigraphic position, colluvial sample NGT-1 could only have originated from one of the sandstone bodies high on the Loskop escarpment (Fig. 3A), all of which overlie the thin ash-fall deposit that yielded the high-precision U-Pb CA-ID-TIMS late Changhsingian age estimate. Age estimates derived from the three clasts range from Roadian to Anisian (Table 1). The oldest nodules from the colluvium sample give Roadian ages, which are consistent with the age of  $267 \pm 3$  Ma from sample NGT9-9. Remnants of middle Permian lakeshore deposits (Prevec et al., 2022), paleosols, and PNC lag deposits (Katsiaficas et al., 2010) are preserved in the Karoo Basin and could have served as a source of the reworked Wordian–Roadian nodules at the Farm Nooitge-dacht section.

The oldest age from sample NGT-1 (268  $\pm$  5 Ma), combined with the youngest age measured from sample NGT9-11 (241  $\pm$  3 Ma),

imply that paleosols with calcite-cemented nodules formed over a period of at least 19 m.y. in the Karoo Basin. Hence, their presence in the uppermost Permian and lowermost Triassic strata in the basin cannot be relied upon to infer a unidirectional trend in aridification, as suggested by some authors (Smith and Botha-Brink, 2014; Botha et al., 2020; Viglietti et al., 2021), nor any other climatic cyclicity (Gastaldo et al., 2020c) without first establishing the ages of individual nodules. In addition, the age of  $247 \pm 8$  Ma from the colluvium sample NGT-1, although imprecise, is consistent with the determination of ages of  $251 \pm 3$  Ma for NGT9-8 and the PNCs higher in the section (Fig. 3C).

Vertebrate biostratigraphy continues to form the basis on which lithostratigraphic units of the Balfour and Katberg formations have been assigned stratigraphic ages (Smith et al., 2020). Geochronometric constraints have been published for only several units augmented by zircon U-Pb geochronology. Rubidge et al. (2013) provided an age estimate of <255.2 Ma for the base of the Dicynodon (= Daptocephalus) AZ from Farm Doornplaats (\$32.035021°, E024.31327°), 32 km northwest of Graaff-Reinet and 55 km from the classic exposures of Upper Permian strata at Old Lootsberg Pass. Here, three detrital zircons, recovered from an ash of unspecified height above the Oudeberg Sandstone Member in the Cistecephalus AZ (Fig. 1), yielded U-Pb CA-ID-TIMS <sup>206</sup>Pb/<sup>238</sup>U Wuchiapingian ages of  $256.32 \pm 0.36$  Ma, and overlapping ages of  $255.24 \pm 0.16$  Ma and  $255.22 \pm 0.16$  Ma. Other analyses of detrital zircon indicate late Paleozoic ages ranging from Mississippian (N = 1;  $330.60 \pm 0.55$  Ma; Serpukhovian), Roadian  $(N = 1; 272.11 \pm 0.24 \text{ Ma})$ , to Capitanian  $(N = 2; 259.66 \pm 0.32 \text{ Ma}, 259.08 \pm 0.15 \text{ Ma}).$ 

A concordant CA-ID-TIMS <sup>206</sup>Pb/<sup>238</sup>U Changhsingian zircon age estimate of  $253.48 \pm 0.15$  Ma was reported from the Elandsberg Member at Old Lootsberg Pass, which was considered then to be in the Dicynodon AZ (= lower Daptocephalus AZ; Gastaldo et al., 2015). At the time, this horizon was considered to lie  $\sim$ 60 m below the vertebrate biozone boundary. A late Changhsingian CA-ID-TIMS <sup>206</sup>Pb/<sup>238</sup>U zircon age of  $252.24 \pm 0.11$  Ma was reported by Gastaldo et al. (2020a) from the Palingkloof Member of the succession at Farm Nooitgedacht near the base of the overlying L. declivis AZ, as then defined by Botha et al. (2020) and Botha and Smith (2020). Farm Nooitgedacht, the locality from which we report new age constraints, is located in a more distal basinal setting, ~195 km to the northeast of Old Lootsberg Pass. Since then, the diagnostic taxa of what were considered to be two discrete biozones were shown to have overlapping stratigraphic ranges (Fig. 1;

Gastaldo et al., 2021). In contrast, Botha et al. (2020) reported a maximum depositional age of  $251.7 \pm 0.3$  Ma (Induan) based on detrital zircon recovered from a mudstone on the Spitskop koppie (1.5 km SSW of Loskop; Fig. 2) on Farm Nooitgedacht. This is  $\sim$ 6.5 m below their biostratigraphic boundary, which they use to infer a latest Changhsingian age (Botha et al., 2020; their fig. 9) for the uppermost Daptocephalus AZ in support of their end-Permian extinction model (but see Gastaldo et al., 2021). To date, no maximum depositional age has been reported for any interval higher in the Beaufort Group, particularly in the Katberg Formation (Fig. 1). Our age results from the PNC deposits provide maximum depositional ages for the Katberg Formation, tightening the stratigraphic ages from Olenekian to Ladinian (Fig. 7). The ages of 249  $\pm$  3 Ma (NGT9-10) and 241  $\pm$  3 Ma (NGT9-11) derived from PNCs near the top of the section imply that the top of the Lystrosaurus declivis AZ, traditionally assigned to the early Olenekian (Lucas, 1998; Botha and Smith, 2020), should be extended to the Ladinian, which indicates the presence of long depositional gaps in the Katberg Formation. Similarly, the overlying Cynognathus Assemblage Zone, generally considered to range from the Olenekian to the late Anisian or early Ladinian (Liu et al., 2017; Hancox et al., 2020), is of much younger age, a hypothesis first advanced by Ottone et al. (2014).

The turnover in the vertebrate-fossil record of the Karoo Basin, from the last appearance data of diagnostic taxa assigned to the Daptocephalus to the first appearance data of diagnostic taxa assigned to the Lystrosaurus declivis AZ, has been used to mark the end-Permian extinction event (Botha et al., 2020, and references therein) and has been applied to other continents in both the southern and northern paleohemispheres (Dal Corso et al., 2022). When Gastaldo et al. (2020a) reported a U-Pb zircon age of 252.24  $\pm$  0.11 Ma at Farm Nooitgedacht, the volcanic ash-fall deposit was considered to lie in the Lystrosaurus declivis AZ based on the paradigm prevailing at that time. Since then, the diagnostic taxa used to delimit each vertebrate biozone as unique were shown to have been coeval during the Changhsingian (Gastaldo et al., 2021). The presence of a palynoassemblage assigned to the Playfordiaspora crenulata biozone from a mudstone in the lowest Katberg sandstone unit on Loskop (Fig. 7; Gastaldo et al., 2020a) is consistent with the Olenekian age estimate from the basal PNC lag.

Recent palynologic studies in Australia, constrained by geochronology, interpret the initial collapse of the glossopterid biome on that landmass to have taken place some 330 k.y. prior to the marine mass extinction event

(Fielding et al., 2019; Mays et al., 2020). These authors suggest that terrestrial ecosystems were impacted earlier than the zenith of marine extinction at 251.902  $\pm$  0.024 Ma (Shen et al., 2019). The collapse of the Glossopteris flora is believed to mark the beginning of the terrestrial crisis in southern Gondwana and is associated with a marked reduction in primary productivity (Mays et al., 2020). The turnover from a Glossopteris-dominated landscape to that of a depauperate flora, dominated by lycopods and peltasperms, is marked by the transition from the Dulhuntyispora parvithola palynozone to the Playfordiaspora crenulata palynozone (Fig. 7; Mays et al., 2021). The boundary between the two biozones is in the latest Changhsingian at  $252.31 \pm 0.07$  Ma (Fielding et al., 2019; Mays et al., 2020). Fielding et al. (2019) indicated two alternate positions for the Permian-Triassic boundary, namely the lower part of the P. crenulata zone based on preliminary CA-ID-TIMS dates and the base of the Lunatisporites pellucides palynozone (which overlies the P. crenulata and the Protohaploxypinus microcorpus palynozones). Mays et al. (2020) give the same estimated chronostratigraphic range of the *P. crenulata* zone in the zone description but, in one of their figures, placed the top of the biozone coincident with the marine Permian-Triassic boundary (Mays et al., 2020; their fig. 1). Vajda et al. (2020; their fig. 2), however, reported an uncertainty about the age of this palynozone, ascribing it neither wholly to the Permian or Triassic, with McLoughlin et al. (2021) placing the Frazier Beach Member, which lies above the extinction crisis, solely in the latest Permian based on geochronological constraints. At the time, the base of the Protohaploxypinus microcorpus was considered to be mid-Induan (Griesbachian, Early Triassic) in age.

More recently, Mays et al. (2021) extended the upper boundary of the P. crenulata palynozone equivalent with the Griesbachian-Dienarian stage boundary (250.4 Ma), with the overlying P. microcorpus palynozone shifted into the younger Dienarian stage (250.4–249.7 Ma). However, Karoo pollen attributable to Glossopteris are present in the P. crenulata palynozone (Fig. 6), which may suggest the temporary persistence of the lineage into the Early Triassic in this basin (Gastaldo et al., 2021). In contrast, the P. crenulata Zone in Eastern Australia is latest Permian, starting at 252.31  $\pm$  0.07 Ma (Fielding et al., 2019), and older than the occurrence of P. crenulata at Farm Nooitgedacht (Gastaldo et al., 2020a). Here, the P. crenulata palynozone occurs in the sandstone body above the PNC horizon. Hence, our result of 251  $\pm$  3 Ma provides a maximum age estimate for the first occurrence of the *P. crenulata* palynozone in this part of the Karoo Basin, and the age overlaps with the interpreted age of the floristic turnover recorded in Eastern Australia (Fig. 7).

The U-Pb date of  $251 \pm 3$  Ma reported for the youngest nodules of the lowermost PNC indicates that the Permian-Triassic boundary at Farm Nooitgedacht may be preserved in strata in the short stratigraphic succession between the ash-fall bed, which was dated at  $252.24 \pm 0.11$  Ma by Gastaldo et al. (2020a), and the base of the overlying sandstone channel (Fig. 7). It is unknown whether these nodules might have formed during the transition between the Permian and Triassic and represent conditions in the basin during the extinction event. However, because these clasts were reworked from calcic vertisols into the PNC during landscape degradation, it is more likely that the Permian-Triassic boundary interval at Farm Nooitgedacht is not preserved.

U-Pb age errors from LA-ICP-MS analyses of nodules can be as low as 1%. This error does not include error in the standard for the same reason that errors in decay constants are normally not included in zircon U-Pb age errors. If everyone uses the same standard (or constants in the case of zircon), the same results should be obtained even though they may not reflect the true accuracy. A great deal more work needs to be done to study factors controlling reproducibility in dating calcites, but this is beyond the scope of this paper. The fact that we have shown that we can reproduce ages of four nodules from each of two hand samples provides some evidence as to the reliability of our quoted precisions.

The results of this study demonstrate that U-Pb dating of pedogenic nodules has the potential to greatly improve our understanding of mass extinction in the terrestrial environment. A 1% age error is an order of magnitude greater than for zircon, but pedogenic carbonate nodules are much more abundant than zirconbearing tuff horizons. Even detrital nodules are useful since they are unlikely to have been transported over large distances. The application of ID-TIMS dating can significantly improve age precision. Furthermore, it has been shown that the relationship between isotopic fractionation of organic and inorganic carbon can serve as a proxy for the partial pressure of CO<sub>2</sub> in the atmosphere at the time of pedogenic carbonate formation (Gastaldo et al., 2014). The application of clumped O-isotope measurements may also allow for estimates of temperature (Methner et al., 2016), thus giving a detailed record of atmospheric changes during critical periods of Earth's history.

#### CONCLUSIONS

The calcite-cemented carbonate nodules derived from a paleosol horizon and pedogenic nodules collected from intraformational conglomerate lag deposits at Farm Nooitgedacht show unusually high-U contents (20–60 ppm), which are often around 1 ppm or less in carbonates (e.g., Li et al., 2014; Roberts et al., 2020). This allows age determinations by LA-ICP-MS to be measured with errors down to  $\sim \! 1\%$ , despite the presence of significant common Pb. Although such errors are much higher than those associated with analyses of zircon, which yields highly radiogenic Pb, they are low enough to be geologically useful, particularly when zircon dating is absent.

The age estimate of  $252 \pm 3$  Ma derived from an in situ paleosol nodule located below a volcanogenic ash-fall deposit is consistent with the high-precision U-Pb CA-ID-TIMS zircon age of 252.24  $\pm$  0.11 Ma (Gastaldo et al., 2020a) of that ash deposit. U-Pb dating of PNC units constrains the age range for the Katberg Formation at Farm Nooitgedacht from Olenekian to Ladinian and implies the need for a revaluation of the age assigned to the overlying Burgersdorp Formation. U-Pb ages for multiple nodules extracted from two samples collected from different locations within the same PNC lag deposit at the base of the Katberg Formation yield overlapping ages (Wuchiapingian-Olenekian). This result suggests that the pedogenic nodule conglomerate consists of sediment derived from a proximal source. The age of  $251 \pm 3$  Ma for the youngest group of nodules represents a maximum age estimate for genesis of the nodules and their deposition as a PNC lag deposit. These results also provide a maximum age estimate for the first occurrence of the P. crenulata palynozone in the Karoo Basin, which has been reported to mark the end-Permian extinction event at Sydney Basin, Australia (Mays et al., 2021).

## ACKNOWLEDGMENTS

We are grateful for constructive comments by Andrew Kylander-Clark and an anonymous reviewer, which greatly improved this manuscript. This work was supported by the Hugh Snyder International Scholarship to H. Rochín-Bañaga and by Natural Sciences and Engineering Research Council of Canada Discovery Grant RGPIN-2016-05575 to D.W. Davis. Research efforts also were supported, in part, by the Council for Geoscience (South Africa), the National Science Foundation Division of Earth Sciences (grants 0749895, 0934077, 1123570, and 1624302), and a Fulbright Scholar Award from the U.S. Department of State to R.A. Gastaldo.

## REFERENCES CITED

Aftabuzzaman, Md., Kaiho, K., Biswas, R.K., Liu, Y., Saito, R., Tian, L., Bhat, G.M., and Chen, Z.-Q., 2021,

- End-Permian terrestrial disturbance followed by the complete plant devastation, and the vegetation protorecovery in the earliest-Triassic recorded in coastal sea sediments: Global and Planetary Change, v. 205, https://doi.org/10.1016/j.gloplacha.2021.103621.
- Barbolini, N., Rubidge, B., and Bamford, M.K., 2018, A new approach to biostratigraphy in the Karoo retroarc foreland system: Utilizing restricted-range palynomorphs and their first appearance datums for correlation: Journal of African Earth Sciences, v. 140, p. 114–133, https://doi.org/10.1016/j.jafrearsci.2017.11.031.
- Benca, J.P., Duijnstee, I.A.P., and Looy, C.V., 2018, UV-B-induced forest sterility: Implications of ozone shield failure in Earth's largest extinction: Science Advances, v. 4, https://doi.org/10.1126/sciadv.1700618.
- Black, B.A., Lamarque, J.F., Shields, C.A., Elkins-Tanton, L.T., and Kiehl, J.T., 2014, Acid rain and ozone depletion from pulsed Siberian traps magmatism: Geology, v. 42, p. 67–70, https://doi.org/10.1130/G34875.1.
- Botha, J., and Smith, R.M.H., 2020, Biostratigraphy of the Lystrosaurus declivis Assemblage Zone (Beaufort Group, Karoo Supergroup), South Africa: South African Journal of Geology, v. 123, p. 207–216, https://doi .org/10.25131/sajg.123.0015.
- Botha, J., Huttenlocker, A.K., Smith, R.M.H., Prevec, R., Viglietti, P., and Modesto, S.P., 2020, New geochemical and palaeontological data from the Permian-Triassic boundary in the South African Karoo Basin test the synchronicity of terrestrial and marine extinctions: Palaeogeography, Palaeoclimatology, Palaeoecology, v. 540, https://doi.org/10.1016/j.palaeo.2019.109467.
- Botha-Brink, J., Huttenlocker, A.K., and Modesto, S.P., 2014, Vertebrate Paleontology of Nooitgedacht 68: A Lystrosaurus maccaigi-rich Permian-Triassic boundary locality in South Africa, in Kammerer, C.F., Angielczyk, K.D., and Fröbisch, J., eds., The Early Evolutionary History of the Synapsida: Dordrecht, Netherlands, Springer, p. 289–304, https://doi.org/10 .1007/978-94-007-6841-3\_17.
- Brand, U., Posenato, R., Came, R., Affek, H., Angiolini, L., Azmy, K., and Farabegoli, E., 2012, The end-Permian mass extinction: A rapid volcanic CO<sub>2</sub> and CH<sub>4</sub>-climatic catastrophe: Chemical Geology, v. 322–323, p. 121– 144, https://doi.org/10.1016/j.chemgeo.2012.06.015.
- Burgess, S.D., and Bowring, S.A., 2015, High-precision geochronology confirms voluminous magmatism before, during, and after Earth's most severe extinction: Science Advances, v. 1, https://doi.org/10.1126/sciadv .1500470.
- Burgess, S.D., Bowring, S., and Shen, S.-Z., 2014, High-precision timeline for Earth's most severe extinction: Proceedings of the National Academy of Sciences of the United States of America, v. 111, no. 9, p. 3316–3321, https://doi.org/10.1073/pnas.1317692111.
- Burgess, S.D., Muirhead, J.D., and Bowring, S.A., 2017, Initial pulse of Siberian Traps sills as the trigger of the end-Permian mass extinction: Nature Communications, v. 8, 164, https://doi.org/10.1038/s41467-017-00083-9.
- Catuneanu, O., Wopfner, H., Eriksson, P.G., Cairncross, B., Rubidge, B.S., Smith, R.M.H., and Hancox, P.J., 2005, The Karoo basins of south-central Africa: Journal of African Earth Sciences, v. 43, p. 211–253, https://doi.org/10.1016/j.jafrearsci.2005.07.007.
- Chen, Z.Q., Yang, H., Luo, M., Benton, M.J., Kaiho, K., Zhao, L., Huang, Y., Zhang, K., Fang, Y., Jiang, H., Qiu, H., Li, Y., Tu, C., Shi, L., Zhang, L., Feng, X., and Chen, L., 2015, Complete biotic and sedimentary records of the Permian–Triassic transition from Meishan section, South China: Ecologically assessing mass extinction and its aftermath: Earth-Science Reviews, v. 149, p. 67–107, https://doi.org/10.1016/j.earscirev 2014.10.005.
- Chu, D., Corso, J.D., Shu, W., Song, H., Wignall, P.B., Grasby, S.E., van de Schootbrugge, B., Zong, K., Wu, Y., and Tong, J., 2021, Metal-induced stress in survivor plants following the end-Permian collapse of land ecosystems: Geology, v. 49, p. 657–661, https://doi.org/10.1130/G48333.1.
- Dal Corso, J., Song, H., Callegaro, S., Chu, Y., Sun, D., Hilton, J., Grasby, S.E., Joachimski, M.M., and Wignall, P.B., 2022, Environmental crises at the Permian-Triassic mass extinction: Nature Reviews: Earth & En-

- vironment, v. 3, p. 197–214, https://doi.org/10.1038/s43017-021-00259-4.
- Davis, D.W., and Rochín-Bañaga, H., 2021, A new Bayesian approach toward improved regression of low-count U-Pb geochronology data generated by LA-ICPMS: Chemical Geology, v. 582, https://doi.org/10.1016/j .chemgeo.2021.120454.
- Davydov, V.I., Karasev, E.V., Nurgalieva, N.G., Schmitz, M.D., Budnikov, I.V., Biakov, A.S., Kuzina, D.M., Silantiev, V.V., Urazaeva, M.N., Zharinova, V.V., Zorina, S.O., Gareev, B., and Vasilenko, D.V., 2021, Climate and biotic evolution during the Permian–Triassic transition in the temperate Northern Hemisphere, Kuznetsk Basin, Siberia, Russia: Palaeogeography, Palaeoclimatology, Palaeoecology, v. 573, https://doi.org/10.1016/j .palaeo.2021.110432.
- Drost, K., Chew, D., Petrus, J.A., Scholze, F., Woodhead, J.D., Schneider, J.W., and Harper, D.A.T., 2018, An image mapping approach to U-Pb LA-ICP-MS carbonate dating and applications to direct dating of carbonate sedimentation: Geochemistry, Geophysics, Geosystems, v. 19, p. 4631–4648, https://doi.org/10 .1029/2018GC007850.
- Erwin, D.H., 1994, The Permo-Triassic extinction: Nature, v. 367, p. 231–236, https://doi.org/10.1038/367231a0.
- Fielding, C.R., Frank, T.D., McLoughlin, S., Vajda, V., Mays, C., Tevyaw, A.P., Winguth, A., Winguth, C., Nicoll, R.S., Bocking, M., and Crowley, J.L., 2019, Age and pattern of the southern high-latitude continental end-Permian extinction constrained by multiproxy analysis: Nature Communications, v. 10, 385, https://doi.org/10 .1038/s41467-018-07934-z.
- Fielding, C.R., Frank, T.D., Tevyaw, A., Savatic, K., Vajda, V., Mcloughlin, S., Mays, C., Nicoll, R.S., Bocking, M., and Crowley, J., 2021, Sedimentology of the continental end Permian extinction event in the Sydney Basin, eastern Australia: Sedimentology, v. 68, p. 30–62, https://doi.org/10.1111/sed.12782.
- Gastaldo, R.A., and Demko, T.M., 2011, Long term hydrology controls the plant fossil record, in Allison, P.A., and Bottjer, D.J., eds., Taphonomy: Processes and Bias through Time (second edition): Dordrecht, Netherlands, Springer, Topics in Geobiology, v. 32, p. 249–286.
- Gastaldo, R.A., Pludow, B.A., and Neveling, J., 2013, Mud aggregates from the Katberg Formation, South Africa: Additional evidence for Early Triassic degradational landscapes: Journal of Sedimentary Research, v. 83, p. 531–540, https://doi.org/10.2110/jsr.2013.45.
- Gastaldo, R.A., Knight, C.L., Neveling, J., and Tabor, N.J., 2014, Latest Permian paleosols from Wapadsberg Pass, South Africa: Implications for Changhsingian climate: Geological Society of America Bulletin, v. 126, p. 665– 679, https://doi.org/10.1130/B30887.1.
- Gastaldo, R.A., Kamo, S.L., Neveling, J., Geissman, J.W., Bamford, M., and Looy, C.V., 2015, Is the vertebratedefined Permian–Triassic boundary in the Karoo Basin, South Africa, the terrestrial expression of the end-Permian marine event?: Geology, v. 43, p. 939–942, https:// doi.org/10.1130/G37040.1.
- Gastaldo, R.A., Neveling, J., Looy, C.V., Bamford, M., Kamo, S.L., and Geissman, J.W., 2017, Paleontology of the Blaauwater 67 and 65 farms, South Africa: Testing the Daptocephalus/Lystrosaurus biozone boundary in a stratigraphic framework: Palaios, v. 32, p. 349–366, https://doi.org/10.2110/palo.2016.106.
- Gastaldo, R.A., Neveling, J., Geissman, J.W., and Kamo, S.L., 2018, A lithostratigraphic and magnetostratigraphic framework in a geochronologic context for a purported Permian-Triassic boundary section at Old (West) Lootsberg Pass, Karoo Basin, South Africa: Geological Society of America Bulletin, v. 130, p. 1411–1438, https://doi.org/10.1130/B31881.1.
- Gastaldo, R.A., Neveling, J., Geissman, J.W., and Li, J., 2019, A multidisciplinary approach to review the vertical and lateral facies relationships of the purported vertebrate-defined terrestrial Permian–Triassic boundary interval at Bethulie, Karoo Basin, South Africa: Earth-Science Reviews, v. 189, p. 220–243, https://doi .org/10.1016/j.earscirev.2017.08.002.
- Gastaldo, R.A., Kamo, S.L., Neveling, J., Geissman, J., Looy, C.V., and Martini, A.M., 2020a, The base of the *Lystrosaurus* Assemblage Zone, Karoo Basin,

- predates the end-Permian marine extinction: Nature Communications, v. 11, 1428, https://doi.org/10.1038/s41467-020-15243-7.
- Gastaldo, R.A., Kus, K., Neveling, J., and Tabor, N., 2020b, Calcic vertisols in the upper Daptocephalus Assemblage Zone, Balfour Formation, Karoo Basin, South Africa: Implications for Late Permian Climate: Journal of Sedimentary Research, v. 90, p. 609–628, https://doi .org/10.2110/isr.2020.32.
- Gastaldo, R.A., Tabor, N., and Neveling, J., 2020c, Trends in Late Permian (Changhsingian) paleoclimate in the Daptocephalus Assemblage Zone, Eastern Cape Province, South Africa: Frontiers in Science, v. 8.
- Gastaldo, R.A., Neveling, J., Geissman, J.W., and Kamo, S.L., 2021, A tale of two Tweefonteins: What physical correlation, magnetostratigraphy, and geochronology say about the end-Permian terrestrial extinction paradigm: Geological Society of America Bulletin, v. 133, p. 691–721, https://doi.org/10.1130/B35830.1.
- Hancox, P.J., Neveling, J., and Rubidge, B.S., 2020, Biostratigraphy of the *Cynognathus* Assemblage Zone (Beaufort Group, Karoo Supergroup), South Africa: South African Journal of Geology, v. 123, no. 2, p. 217–238, https://doi.org/10.25131/sajg.123.0016.
- Hermann, E., Hochuli, P.A., Bucher, H., Brühwiler, T., Hautmann, M., Ware, D., and Roohi, G., 2011, Terrestrial ecosystems on North Gondwana following the end-Permian mass extinction: Gondwana Research, v. 20, p. 630–637, https://doi.org/10.1016/j.gr.2011.01.008.
- Hill, C.A., Polyak, V.J., Asmerom, Y., and Provencio, P., 2016, Constraints on a Late Cretaceous uplift, denudation, and incision of the Grand Canyon region, southwestern Colorado Plateau, USA, from U-Pb dating of lacustrine limestone: Tectonics, v. 35, p. 896–906, https://doi.org/10.1002/2016TC004166.
- Hoareau, G., Claverie, F., Pecheyran, C., Paroissin, C., Grignard, P.-A., Motte, G., Chailan, O., and Girard, J.-P., 2021, Direct U-Pb dating of carbonates from micronscale femtosecond laser ablation inductively coupled plasma mass spectrometry images using robust regression: Geochronology, v. 3, p. 67–87, https://doi.org/10.5194/gchron-3-67-2021.
- Jaffey, A.H., Flynn, K.F., Glendenin, L.E., Bentley, W.C., and Essling, A.M., 1971, Precision measurement of the half-lives and specific activities of <sup>235</sup>U and <sup>238</sup>U: Physical Review, v. C4, p. 1889–1906.
- Jahn, B., and Cuvellier, H., 1994, Pb-Pb and U-Pb geochronology of carbonate rocks: An assessment: Chemical Geology, v. 115, p. 125–151, https://doi.org/10.1016/ /0009-2541(94)90149-X.
- Joachimski, M.M., Müller, J., Gallagher, T.M., Mathes, G., Chu, D.L., Mouraviev, F., Silantiev, V., Sun, Y.D., and Tong, J.N., 2022, Five million years of high atmospheric CO<sub>2</sub> in the aftermath of the Permian–Triassic mass extinction: Geology, v. 50, p. 650–654, https://doi.org/10.1130/G49714.1.
- Kamo, S.L., Czamanske, G.K., Amelin, Y., Fedorenko, V.A., Davis, D.W., and Trofimov, V.R., 2003, Rapid eruption of Siberian flood-volcanic rocks and evidence for coincidence with the Permian–Triassic boundary and mass extinction at 251 Ma: Earth and Planetary Science Letters, v. 214, p. 75–91, https://doi.org/10.1016 /S0012-821X(03)00347-9.
- Katsiaficas, N., Gastaldo, R.A., and Neveling, J., 2010, An analysis of geometric and sedimentologic characteristics of a middle Permian fluvial system, Karoo Basin, South Africa: Geological Society of America Abstracts with Program, v. 42, no. 5, p. 428.
- Knoll, A.H., Bambach, R.K., Canfield, D.E., and Grotzinger, J.P., 1996, Comparative Earth history and Late Permian mass extinction: Science, v. 273, p. 452–457, https://doi. org/10.1126/science.273.5274.452.
- Leone, G., Bonadonna, F., and Zanchetta, G., 2000, Stable isotope record in mollusca and pedogenic carbonate from late Pliocene soils of Central Italy: Palaeogeography, Palaeoclimatology, Palaeoecology, v. 163, p. 115–131, https://doi.org/10.1016 /S0031-0182(00)00148-6.
- Li, Q., Parrish, R.R., Horstwood, M.S.A., and McArthur, J.M., 2014, U-Pb dating of cements in Mesozoic ammonites: Chemical Geology, v. 376, p. 76–83, https:// doi.org/10.1016/j.chemgeo.2014.03.020.

- Liu, J., Ramezani, J., Lu, L., Shang, Q.-H., Xu, G.-H., Wang, Y.-Y., and Yang, J.-S., 2017, High-precision temporal calibration of Middle Triassic vertebrate biostratigraphy: U-Pb zircon constraints for the Sinokannemeyeria Fauna and Yonghesuchus: Vertebrata PalAsiatica, v. 55, p. 1–9.
- Looy, C.V., Twitchett, R.J., Dilcher, D.L., Van Konijnenburg-Van Cittert, J.H., and Visscher, H., 2001, Life in the end-Permian dead zone: Proceedings of the National Academy of Sciences of the United States of America, v. 98, p. 7879–7883, https://doi.org/10.1073/pnas .131218098.
- Lucas, S., 2021, Nonmarine mass extinctions: Paleontological Research, v. 25, p. 329–344, https://doi.org/10.2517 /2021PR004.
- Lucas, S.G., 1998, Global Triassic tetrapod biostratigraphy and biochronology: Palaeogeography, Palaeoclimatology, Palaeoecology, v. 143, p. 347–384, https://doi.org /10.1016/S0031-0182(98)00117-5.
- Ludwig, K.R., 2012, User's Manual for Isoplot 3.75: A Geochronological Toolkit for Microsoft Excel: Berkeley Geochronological Center Special Publication 4, 75 p.
- Mays, C., Vajda, V., Frank, T.D., Fielding, C.R., Tevyaw, A.P., and McLoughlin, S., 2020, Refined Permian– Triassic floristic timeline reveals early collapse and delayed recovery of south polar terrestrial ecosystems: Geological Society of America Bulletin, v. 132, p. 1489–1513, https://doi.org/10.1130/B35355.1.
- Mays, C., McLoughlin, S., Frank, T.D., Fielding, C.R., Slater, S.M., and Vajda, V., 2021, Lethal microbial blooms delayed freshwater ecosystem recovery following the end-Permian extinction: Nature Communications, v. 12, 5511, https://doi.org/10.1038/s41467-021-25711-3.
- McLoughlin, S., Nicoll, R.S., Crowley, J.L., Vajda, V., Mays, C., Fielding, C.R., Frank, T.D., Alexander, W., and Bocking, M., 2021, Age and paleoenvironmental significance of the Frazer Beach Member—A new lithostratigraphic unit overlying the end-Permian extinction horizon in the Sydney Basin, Australia: Frontiers of Earth Science, v. 8.
- Methner, K., Mulch, A., Fiebig, J., Wacker, U., Gerdes, A., Graham, S.A., and Chamberlain, C.P., 2016, Rapid Middle Eocene temperature change in western North America: Earth and Planetary Science Letters, v. 450, p. 132–139, https://doi.org/10.1016/j.epsl.2016.05.053.
- Nowak, H., Schneebeli-Hermann, E., and Kustatscher, E., 2019, No mass extinction for land plants at the Permian–Triassic transition: Nature Communications, v. 10, p. 1–8, https://doi.org/10.1038/s41467-018-07945-w.
- Ogg, J.G., 2012, Triassic, in Gradstein, F.M., Ogg, J.G., Schmitz, M., and Ogg, G., eds., The Geologic Time Scale 2012: Amsterdam, Netherlands, Elsevier, p. 681–730, https://doi.org/10.1016/B978-0-444-59425-9.00025-1.
- Ottone, E.G., Monti, M., Marsicano, C.A., de la Fuente, M.S., Naipauer, M., Armstrong, R., and Mancuso, A.C., 2014, A new Late Triassic age for the Puesto Viejo Group (San Rafael depocenter, Argentina): SHRIMP U-Pb zircon dating and biostratigraphic correlations across southern Gondwana: Journal of South American Earth Sciences, v. 56, p. 186–199, https://doi.org/10.1016/j.jsames.2014.08.008.
- Pace, D.W., Gastaldo, R.A., and Neveling, J., 2009, Early Triassic aggradational and degradational landscapes of the Karoo Basin and evidence for climate oscillation following the P-Tr Event: Journal of Sedimentary Research, v. 79, p. 316–331, https://doi.org/10.2110/jsr .2009.036.
- Prevec, R., Gastaldo, R.A., Neveling, J., Reid, S.B., and Looy, C.V., 2010, An autochthonous Glossoperid flora with latest Permian palynomorphs and its depositional setting from the *Dicynodon* Assemblage Zone of the southern Karoo Basin, South Africa: Palaeogeography, Palaeoclimatology, Palaeoecology, v. 292, p. 391–408, https://doi.org/10.1016/j.palaeo.2010.03.052.
- Prevec, R., Nel, A., Day, M.O., Muir, R.A., Matiwane, A., Kirkaldy, A.P., Moyo, S., Staniczek, A., Cariglino, B., Maseko, Z., Kom, N., Rubidge, B.S., Garrouste, R., Holland, A., and Barber-James, H.M., 2022, South African Lagerstätte reveals middle Permian Gondwanan lakeshore ecosystem in exquisite detail: Communications Biology, v. 5, 1154, https://doi.org/10.1038 /s42003-022-04132-y.

- Railsback, B.L., 2021, Pedogenic carbonate nodules from a forested region of humid climate in central Tennessee, USA, and their implications for interpretation of C<sub>3</sub>-C<sub>4</sub> relationships and seasonality of meteoric precipitation from carbon isotope (δ<sup>13</sup>C) data: Catena, v. 200, https:// doi.org/10.1016/j.catena.2021.105169.
- Rasbury, E.T., and Cole, J.M., 2009, Directly dating geologic events: U-Pb dating of carbonates: Reviews of Geophysics, v. 47, https://doi.org/10.1029/2007RG000246.
- Rasmussen, C., Mundil, R., Irmis, R.B., Geisler, D., Gehrels, G.E., Olsen, P.E., Kent, D.V., Lepre, C., Kinney, S.T., Geissman, J.W., and Parker, W.G., 2021, U-Pb zircon geochronology and depositional age models for the Upper Triassic Chinle Formation (Petrified Forest National Park, Arizona, USA): Implications for Late Triassic paleoecological and paleoenvironmental change: Geological Society of America Bulletin, v. 133, p. 539–558, https://doi.org/10.1130/B35485.1.
- Retallack, G.J., 2005, Pedogenic carbonate proxies for amount and seasonality of precipitation in paleosols: Geology, v. 33, p. 333–336, https://doi.org/10.1130 /G21263.1.
- Retallack, G.J., Satoshi, T.B., and Timothy, T., 2002, Late Miocene advent of tall grassland paleosols in Oregon: Palaeogeography, Palaeoclimatology, Palaeoecology, v. 183, p. 329–354, https://doi.org/10 .1016/S0031-0182(02)00250-X.
- Roberts, N.M.W., Rasbury, E.T., Parrish, R.R., Smith, C.J., Horstwood, M.S.A., and Condon, D.J., 2017, A calcite reference material for LA-ICP-MS U-Pb geochronology: Geochemistry, Geophysics, Geosystems, v. 18, p. 2807–2814, https://doi.org/10.1002/2016GC006784.
- Roberts, N.M.W., Drost, K., Horstwood, M.S.A., Condon, D.J., Chew, D., Drake, H., Milodowski, A.E., McLean, N.M., Smye, A.J., Walker, R.J., Haslam, R., Hodson, K., Imber, J., Beaudoin, N., and Lee, J.K., 2020, Laser ablation inductively coupled plasma mass spectrometry (LA-ICP-MS) U-Pb carbonate geochronology: Strategies, progress, and limitations: Geochronology, v. 2, no. 1, p. 33–61, https://doi.org/10.5194/gchron-2-33-2020.
- Rubidge, B.S., Erwin, D.H., Ramezani, J., Bowring, S.A., and de Klerk, W.J., 2013, High-precision temporal calibration of Late Permian vertebrate biostratigraphy: U-Pb zircon constraints from the Karoo Supergroup, South Africa: Geology, v. 41, p. 363–366, https://doi .org/10.1130/G33622.1.
- Sheldon, N.D., and Tabor, N.J., 2009, Quantitative paleoenvironmental and paleoclimatic reconstruction paleosols: Earth-Science Reviews, v. 95, p. 1–52, https://doi.org/10.1016/j.earscirev.2009.03.004.
- Shen, S.-Z., Ramezani, J., Chen, J., Cao, C.-Q., Erwin, D.H., Zhang, H., Xiang, L., Schoepfer, S.D., Henderson, C.M., Zheng, Q.-F., Bowring, S.A., Wang, Y., Li, X.-H., Wang, X.-D., Yuan, D.-X., Zhang, Y.-C., Mu, L., Wang, J., and Wu, Y.-S., 2019, A sudden end-Permian mass extinction in South China: Geological Society of America Bulletin, v. 131, p. 205–223, https://doi.org/10.1130/B31909.1.

- Smith, R.M.H., and Botha-Brink, J., 2014, Anatomy of a mass extinction: Sedimentological and taphonomic evidence for drought-induced die-offs at the Permian– Triassic boundary in the main Karoo Basin, South Africa: Palaeogeography, Palaeoclimatology, Palaeoecology, v. 396, p. 99–118, https://doi.org/10.1016/j.palaeo.2014.01.002.
- Smith, R.M.H., Rubidge, B.S., Day, M.O., and Botha, J., 2020, Introduction to the tetrapod biozonation of the Karoo Supergroup: South African Journal of Geology, v. 123, p. 131–140, https://doi.org/10.25131/sajg.123.0009.
- Smith, R.M.H., Botha, J., and Viglietti, P.A., 2022, Taphonomy of drought afflicted tetrapods in the Early Triassic Karoo Basin, South Africa: Palaeogeography, Palaeoclimatology, Palaeoecology, v. 604, https://doi.org/10.1016/j.palaeo.2022.111207.
- Stacey, J.S., and Kramers, J.D., 1975, Approximation of terrestrial lead isotope evolution by two stage model: Earth and Planetary Science Letters, v. 26, p. 207–221, https://doi.org/10.1016/0012-821X(75)90088-6.
- Steiger, R.H., and Jäger, E., 1977, Subcommission on Geochronology: Convention on the use of decay constants in geo- and cosmochronology: Earth and Planetary Science Letters, v. 36, p. 359–362, https://doi.org/10.1016 //0012-821X/77)90060-7.
- Tabor, N.J., Montañez, I.P., Steiner, M.B., and Schwindt, D., 2007, 8<sup>13</sup>C values of carbonate nodules across the Permian–Triassic boundary in the Karoo Supergroup (South Africa) reflect a stinking sulfurous swamp, not atmospheric CO<sub>2</sub>: Palaeogeography, Palaeoclimatology, Palaeoecology, v. 252, p. 370–381, https://doi.org /10.1016/j.palaeo.2006.11.047.
- Tabor, N.J., Geissman, J.W., Renne, P.R., Mundil, R., Mitchell, W.S., III, Myers, T.S., Jackson, J., Looy, C.V., and Kirchholtes, R.P., 2022, Evidence of a Continuous Continental Permian–Triassic Boundary Section in western Equatorial Pangea, Palo Duro Basin, Northwest Texas, U.S.A: Frontiers in Earth Science, v. 9, https://doi.org/10.3389/feart.2021.747777.
- Twitchett, R.J., Looy, C.V., Morante, R., Visscher, H., and Wignall, P.B., 2001, Rapid and synchronous collapse of marine and terrestrial ecosystems during the end-Permian biotic crisis: Geology, v. 29, p. 351–354, https:// doi.org/10.1130/0091-7613(2001)029<0351:RASC OM>2.0.CO;2.
- Vajda, V., McLoughlin, S., Mays, C., Frank, T.D., Fielding, C.R., Tevyaw, A., Lehsten, V., Bocking, M., and Nicoll, R.A., 2020, End-Permian (252 Mya) deforestation, wildfires and flooding—An ancient biotic crisis with lessons for the present: Earth and Planetary Science Letters, v. 529, https://doi.org/10.1016/j.epsl.2019.115875.
- Viglietti, P.A., Smith, R.M.H., Angielczyk, K.D., Kammerer, C.F., Frobisch, J., and Rubidge, B.S., 2016, The *Dapto-cephalus* Assemblage Zone (Lopingian), South Africa: A proposed biostratigraphy based on a new compilation of stratigraphic ranges: Journal of African Earth Sciences, v. 113, p. 153–164, https://doi.org/10.1016/j.jafrearsci.2015.10.011.

- Viglietti, P.A., Rubidge, B.S., and Smith, R.M.H., 2017, New Late Permian tectonic model for South Africa's Karoo Basin: Foreland tectonics and climate change before the end-Permian crisis: Scientific Reports, v. 7, https://doi .org/10.1038/s41598-017-09853-3.
- Viglietti, P.A., et al., 2021, Evidence from South Africa for a protracted end-Permian extinction on land: Proceedings of the National Academy of Sciences of the United States of America, v. 118, https://doi.org/10.1073/pnas 2017045118.
- Visscher, H., Looy, C.V., Collinson, M.E., Brinkhuis, H., Van Konijnenburg-Van Cittert, J.H., Kürschner, W.M., and Sephton, M.A., 2004, Environmental mutagenesis during the end-Permian ecological crisis: Proceedings of the National Academy of Sciences of the United States of America, v. 101, p. 12,952–12,956, https://doi.org/10 .1073/pnas.0404472101.
- Ward, P.D., Montgomery, D.R., and Smith, R.M.H., 2000, Altered river morphology in South Africa related to the Permian-Triassic extinction: Science, v. 289, p. 1740-1743, https://doi.org/10.1126/science.289 .5485.1740.
- Ward, P.D., Botha, J., Buick, R., Dekock, M.O., Erwin, D.H., Garrison, G., Kirschvink, J., and Smith, R.H.M., 2005, Abrupt and gradual extinction among Late Permian land vertebrates in the Karoo Basin, South Africa: Science, v. 307, p. 709–714, https://doi.org/10 .1126/science.1107068.
- Wu, Q., Ramezani, J., Zhang, H., Wang, J., Zeng, F., Zhang, Y., Liu, F., Chen, J., Cai, Y., Hou, Z., Liu, C., Yang, W., Henderson, C.M., and Shen, S.-z., 2021a, Highprecision U-Pb age constraints on the Permian floral turnovers, paleoclimate change, and tectonics of the North China block: Geology, v. 49, p. 677–681, https:// doi.org/10.1130/G48051.1.
- Wu, Y., Chu, D., Tong, J., Song, H., Dal Corso, J., Wignall, P.B., Song, H., Du, Y., and Cui, Y., 2021b, Six-fold increase of atmospheric pCO<sub>2</sub> during the Permian–Triassic mass extinction: Nature Communications, v. 12, https://doi.org/10.1038/s41467-021-22298-7.
- Yang, W., Wan, M., Crowley, J.L., Wang, J., Luo, X., Tabor, N.J., Angeilczyk, K.D., Gastaldo, R.A., Geissman, J.W., Liu, F., Roopnarine, P., and Sidor, C., 2021, Paleoenvironmental and paleoclimatic evolution and cyclo- and chrono-stratigraphy of Upper Permian–Lower Triassic fluvial-lacustrine deposits in Bogda Mountains, NW China—Implications for diachronous plant evolution across the Permian–Triassic boundary: Earth-Science Reviews, v. 222, https://doi.org/10.1016/j.earscirev.2021.103741.

SCIENCE EDITOR: BRAD SINGER ASSOCIATE EDITOR: TROY RASBURY

Manuscript Received 6 February 2023 Revised Manuscript Received 8 May 2023 Manuscript Accepted 22 June 2023

Printed in the USA